

Article

# Experimental Study on Residual Bending Strength of Corroded Reinforced Concrete Beam Based on Micromagnetic Sensor

Jianting Zhou <sup>1,\*</sup>, Junli Qiu <sup>1</sup>, Yingxin Zhou <sup>2</sup>, Yi Zhou <sup>3</sup> and Runchuan Xia <sup>1</sup> 

<sup>1</sup> College of Civil Engineering, Chongqing Jiaotong University, Chongqing 400074, China; 622170086071@mails.cqjtu.edu.cn (J.Q.); rcxia@mails.cqjtu.edu.cn (R.X.)

<sup>2</sup> Yunnan Wuyi Expressway Construction Command, Kunming 650000, China; zyx668@126.com

<sup>3</sup> Chongqing Yapai Bridge Engineering Quality Inspection Co., Ltd., Chongqing 401120, China; boatzy@163.com

\* Correspondence: jtzhou@cqjtu.edu.cn; Tel.: +86-023-6280-2814

Received: 3 July 2018; Accepted: 9 August 2018; Published: 11 August 2018



**Abstract:** This paper presents a nondestructive test method to evaluate the residual bending strength of corroded reinforced concrete beam by analyzing the self-magnetic flux leakage (SMFL) signals. The automatic scanning device was equipped with a micromagnetic sensor and sensor-based experimental details were introduced. Next, the theoretical formula of the normal component  $H_S(z)$  of the SMFL signal that originated from the corroded region was derived based on the magnetic dipole model and the experimental results were discussed. The results indicate that the experimental data of  $H_S(z)$  are consistent with the theoretical calculations, both location and extent of the steel bars corrosion can be qualitatively determined by using  $H_S(z)$ . The gradient  $K$  of  $H_S(z)$  is approximately linearly related to the loss rate,  $S$ , of the bending strength, which can be used to evaluate the residual bending strength of the corroded reinforced concrete beam. This work lays the foundation for evaluating the residual bending strength of corroded reinforced concrete beams using the SMFL signal; the micromagnetic sensor is further applied to the civil engineering.

**Keywords:** corroded reinforced concrete beam; bending strength; micromagnetic sensor; self-magnetic flux leakage; magnetic dipole model

## 1. Introduction

Reinforced concrete structures are widely used in civil engineering due to their high bearing capacity, low cost, and easy construction. However, long-term exposure to the external aggressive environment, means that the reinforcement steel bars of the reinforced concrete structure will be corroded inevitably. The steel corrosion will lead to reduction of the steel bar cross-section, failure of the bond between the steel bar and the concrete, and deterioration of the concrete, which will ultimately weaken the bearing capacity and durability of the reinforced concrete structure [1–3]. Therefore, the measurement of corroded steel bar is crucial to determine the bearing capacity and durability of the reinforced concrete structures.

In the past, traditional electrochemical methods were used to measure corrosion of steel bars, but there are many limitations with these methods. In recent years, smart sensor-based methods that are useful to measure different defects (corrosion, cracks, etc.) of ferromagnetic materials (steel bars, etc.) and other materials have become increasingly popular, such as fiber optic coil winding [4], fiber Bragg grating [5,6], laser scanning technology [7], line scanning thermography (LST) [8,9], inductive thermography [10,11], optical excitation thermography [12], and other thermographic methods [13]

such as acoustic emission and ultrasound testing using traditional and novel transducers [14,15]. Especially, the electromagnetic nondestructive test (NDT) including magnetic flux leakage (MFL) [16], metal magnetic memory (MMM) [17], magnetic acoustic emission (MAE) [18], magnetic Barkhausen noise (MBN) [19], and self-magnetic flux leakage (SMFL) [20] are widely used to measure corrosion and defects of ferromagnetic materials.

Based on the magnetic mechanical effect in the weak magnetic field, factors such as stress and defects within the ferromagnetic material will cause SMFL on its surface by orienting the magnetic domains, dislocating the lattices, and distorting the magnetic field lines [20,21]. Steel bars are a typical kind of ferromagnetic material; the corrosion of steel bars will reduce the bearing capacity and change the SMFL signals of the reinforced concrete structure at the same time. Based on this unified change, the relationship between the bearing capacity and the SMFL signals of corroded reinforced concrete structure can be established. Compared with MFL, SMFL has the advantages of rapid, effective, and simpler operation without any external excitation magnetic field required [22]. Liu [23–25] established a full electronic potential magneto-mechanical model of the ferromagnetic material and explored the relationship between magnetic memory signal and the stress concentration defects. Zhang [26,27] studied the relationship between the SMFL signals and the corrosion extent of corroded reinforced concrete. Zhang [28] investigated the fundamental relationship between corrosion rate and magnetic induction surrounding steel reinforcement. N. Polydorides [29] realized the magnetic induction tomography scanning of corroded reinforced concrete columns. Sun [30] had quantitatively studied the magnetic anomalies of reinforcement rods in bored in situ concrete piles for the first time and summarized their magnetic anomaly character. A. Orbe [31] proposed a magnetic scanning methodology to infer, nondestructively, the spatial dispersion of mechanical properties throughout the steel fiber reinforced concrete (SFRC) structure. H.-J Krause [32] developed a four-channel SQUID system based on magnetometers for detection of tendon ruptures in prestressed members of bridges. B.T. Fernandes [33] described a method of extracting positional information from images of steel bars embedded in concrete using a set of image preprocessing algorithms combined with a modified Hough transform. Chen [34] studied the corrosion of steel bars in reinforced concrete columns based on MFL. However, experimental study of the relationship between the bending strength and SMFL signals of corroded reinforced concrete beam is rarely reported.

In this paper, by detecting and analyzing the bending strength and SMFL signals of the corroded reinforced concrete beam, not only the location and extent of corrosion can be determined, but also the relationship between the bending strength and the SMFL signals. It will provide a rapid, effective, and simpler operation NDT method for the bending strength of corroded reinforced concrete beams.

## 2. Experimental Details and Theoretical Background

### 2.1. Experimental Details Based on Micromagnetic Sensor

To carry out the experiment, 10 identical reinforced concrete tested beams, numbered 1–10, were prepared. In order to explore the relationship between the bending strength and the SMFL signals of the corroded reinforced concrete tested beams more intuitively, central sections (corrosion region) of the tested beams were only reinforced with two tensile steel bars. Ordinary Portland cement, coarse aggregate (stone), with a maximum size of 22 mm, water, and sand were used to mix concrete, the detailed material parameters and dimensional drawings of the tested beam are shown in Table 1 and Figure 1. An electrochemical method [35] was used to corrode steel bars of the tested beams, and the amount of corroded iron could be calculated according to the Faraday's 1st Law, as expressed in Equation (1):

$$\Delta m = \frac{M}{nF} \Delta Q = \frac{M}{nF} I \Delta t \quad (1)$$

where  $\Delta m$  is the amount of corroded iron,  $M$  is the molar mass of iron (Fe),  $n$  is the valence state of  $\text{Fe}^{2+}$ ,  $F$  is the Faraday constant,  $\Delta Q$  is the quantity of electric charge,  $I$  is the direct current flow through steel

bars, and  $\Delta t$  is the corrosion time. The corrosion region is located at the midpoint of the tested beam with a width of approximately 15 cm, wrapped with a towel impregnated with a 5% sodium chloride solution and kept moist by the capillary action. The carbon rod placed in the solution is connected to the negative pole of the current source, and the steel bars are connected to the positive pole, forming a closed circuit for corrosion. Corrosion parameters of all tested beams are presented in Table 2, the layout of the corroding device is shown in Figure 2.

Table 1. Material parameters of tested beam.

Item	Label	Material	Cement	Water	Sand	Stone	Standard Strength (Mpa)	Design Strength (Mpa)
Concrete	C30	Unit dosage (kg/m <sup>3</sup> )	461	175	512	1252	$f_{ck} = 20.1$	$f_{cd} = 14.3$
		weight ratio	1	0.38	1.11	2.72	$f_{tk} = 2.01$	$f_{td} = 1.43$
Item	Reinforcement						Yield Strength (Mpa)	Design Strength (Mpa)
Steel bars	Tensile bars: 2Φ14; Stirrup: Φ8@100						$f_{yk} = 335$	$f_{yd} = 300$

Table 2. Corrosion parameters of all tested beams.

Parameter	No.									
	1#	2#	3#	4#	5#	6#	7#	8#	9#	10#
Corrosion current/A	1.05	1.05	1.05	1.05	1.05	1.05	1.05	1.05	1.05	1.05
Corrosion time/h	0	12	24	36	48	72	96	120	156	504
$\Delta m/g$	0	13.1	26.3	39.4	52.5	78.8	96.9	121.2	157.5	206.0

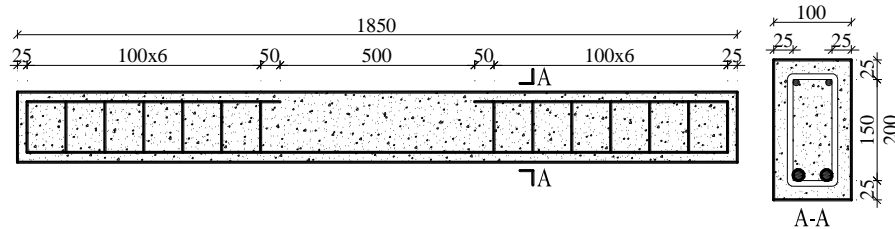


Figure 1. Dimensions of the tested beam (unit: mm).



Figure 2. Layout of the corrosion device.

Each tested beam was corroded in a periodic manner until the corrosion was completed. After each period of corrosion was completed, the SMFL signals of the tested beam were measured and collected. The self-designed 3-dimensional (3D) device for SMFL signals acquisition based on the 3D mechanical displacement system and the high-precision micromagnetic sensor is shown in Figure 3. HMR2300 magnetometer (Honeywell International, Morristown, NJ, USA) was used as the micromagnetic sensor with a resolution to less than  $70 \mu\text{Gs}$ . The device was connected to a computer and can measure the 3D spatial magnetic signal with a controllable scanning speed and path, and then output a data file that contains  $X$ ,  $Y$ , and  $Z$  coordinates and its corresponding magnetic signals components  $H_p(y)$ ,  $H_p(x)$ ,  $H_p(z)$ . The top surface midline of the tested beam is defined as the scanning path for SMFL signals measurement using the 3D scanning device, which is shown in Figure 4. In addition, Figure 4 also shows the different scanning lift-off heights (LFH) from 5 mm to 810 mm.

All the tested beams were subjected to the “4-point” bending test after the corrosion and SMFL signals acquisition were all completed. The layout of the “4-point” bending test is shown in Figure 5.

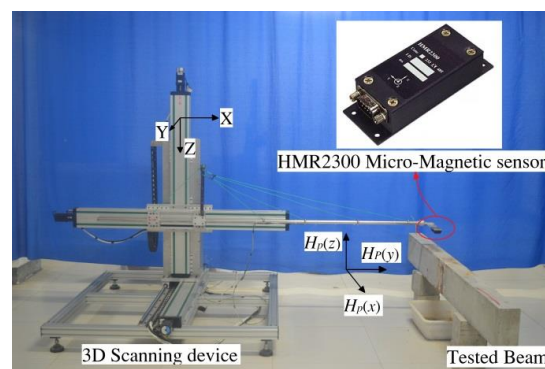


Figure 3. The 3D scanning device for magnetic field measurement.

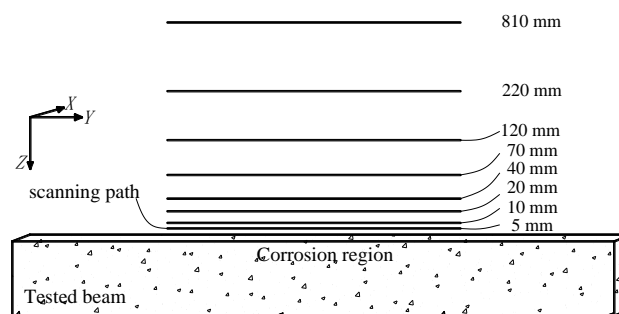


Figure 4. The scanning path of the tested beams to acquire self-magnetic flux leakage (SMFL) signals.

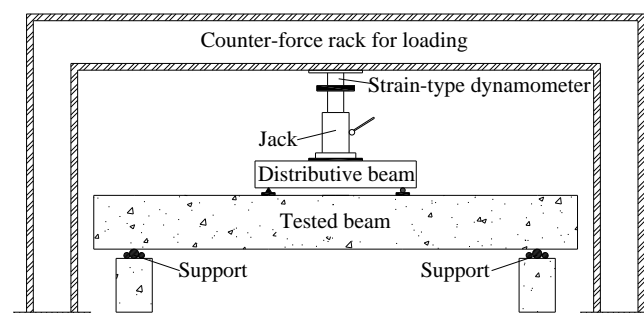


Figure 5. Layout of the “4-point” bending test.

## 2.2. Theoretical Background Based on Magnetic Dipole Model

The equivalent magnetic dipole is a physical model commonly used in the theoretical study of the mechanism of SMFL signal of the ferromagnet [22,27,36]. According to the equivalent magnetic charge theory, the exterior magnetic field including SMFL would be considered to originate from the magnetic charge:  $\rho = -\nabla M$ .  $M$  is the magnetization satisfying  $M = (\mu_r - 1) H_{mL}$ , where  $\mu_r$  is the relative magnetic permeability and the Weiss field  $H_{mL}$  is the effective field producing self-magnetization in the ferromagnet. Figure 6 shows the calculated diagram of the corroded steel bars of the tested beam based on the magnetic dipole model. The corrosion notch of the steel bar is assumed to a rectangular pit with dimensions of  $2b \times h$  and the distribution of charge density  $\pm\rho_{ms}$  at the edges of the corroded region is considered as uniform for simplicity.

Based on the calculated diagram shown in Figure 6, the surface SMFL signal at point  $P(x, y, z)$  due to these concentrated magnetic charges can be expressed as in Equation (2), and its normal component  $dH_p(z)$  can be expressed as in Equation (3):

$$\vec{dH}_P = \sum_{i=1}^4 d\vec{H}_{Pi} = \sum_{i=1}^4 \frac{\pm\rho_{ms} \cdot dh}{2\pi\mu_0 r_i^2} \vec{r}_i \quad (2)$$

$$\begin{cases} dH_{P1}(z) = \frac{(-\rho_{ms}) \cdot (z+h) dh}{2\pi\mu_0 [(x+a)^2 + (y-b)^2 + (z+h)^2]} \\ dH_{P2}(z) = \frac{(+\rho_{ms}) \cdot (z+h) dh}{2\pi\mu_0 [(x+a)^2 + (y+b)^2 + (z+h)^2]} \\ dH_{P3}(z) = \frac{(-\rho_{ms}) \cdot (z+h) dh}{2\pi\mu_0 [(x-a)^2 + (y-b)^2 + (z+h)^2]} \\ dH_{P4}(z) = \frac{(+\rho_{ms}) \cdot (z+h) dh}{2\pi\mu_0 [(x-a)^2 + (y+b)^2 + (z+h)^2]} \end{cases} \quad (3)$$

where  $r_i$  is the space vector from the magnetic charge element to the space point  $P(x, y, z)$ ;  $\mu_0 = 1.0$  is the vacuum magnetic permeability;  $a$  is half of the spacing of the two parallel steel bars, and  $z$  is the lift-off height (LFH). Then, the normal component  $H_p(z)$ , expressed in Equation (4), can be obtained by the integral of Equation (3). The theoretical calculation results of Equation (4) are shown in Figure 7.

It can be seen from Figure 7 that as the corrosion extent increases ( $h$  increases), the amplitude of  $H_p(z)$  increases continuously. While the  $H_p(z)$  amplitude decreases with increasing  $z$  when the corrosion amount  $\Delta m$  is constant. The  $H_p(z)$  curves has a zero-crossing intersection at the midpoint of the corroded region, and the peak-valley spacing equals the corrosion width  $2b$ .

$$\begin{aligned} H_p(z) &= \sum_{i=1}^4 \int_{-h}^0 dH_{Pi}(z) \\ &= \frac{\rho_{ms}}{4\pi\mu_0} \left( \ln \frac{(x+a)^2 + (y-b)^2 + (z-h)^2}{(x+a)^2 + (y-b)^2 + z^2} + \ln \frac{(x+a)^2 + (y+b)^2 + z^2}{(x+a)^2 + (y+b)^2 + (z-h)^2} \right. \\ &\quad \left. + \ln \frac{(x-a)^2 + (y-b)^2 + (z-h)^2}{(x-a)^2 + (y-b)^2 + z^2} + \ln \frac{(x-a)^2 + (y+b)^2 + z^2}{(x-a)^2 + (y+b)^2 + (z-h)^2} \right) \\ &= A \frac{\rho_{ms}}{4\pi\mu_0} \end{aligned} \quad (4)$$

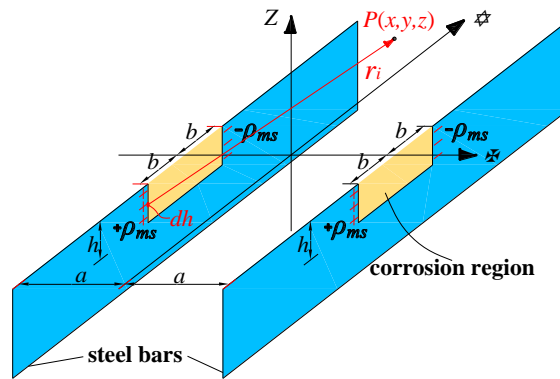


Figure 6. Calculated diagram based on the magnetic dipole model.

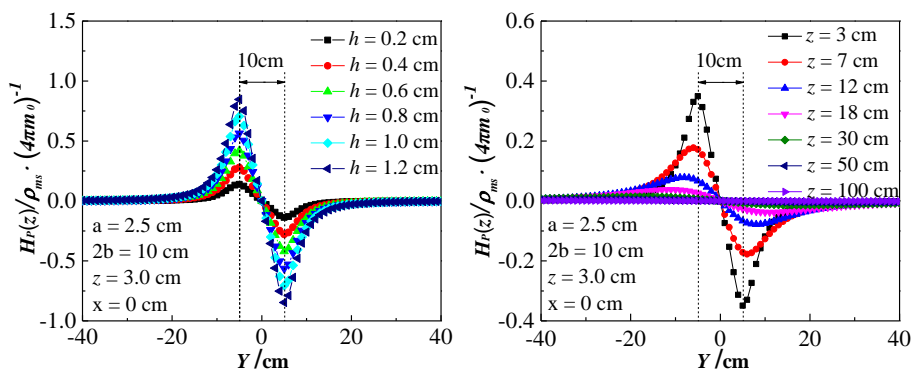


Figure 7. The theoretical calculation results of Equation (4).

### 3. Results and Discussion

#### 3.1. Experimental Measurement Results of SMFL Signal

Figure 8 shows the normal component  $H_p(z)$  curves of the nine tested beam SMFL signals with different corrosion amounts  $\Delta m$ , where  $Y = 400\sim 550$  mm corresponds to the corrosion region. The big spikes of amplitude outside of the corrosion region in Figure 8 are due to the effect of stirrups. As the corrosion amount  $\Delta m$  increased, the amplitude of the  $H_p(z)$  curves in the corroded region increased, and then developed obvious peak-to-valley values and intersection; the smaller the LFH is, the larger the amplitude of  $H_p(z)$  in the corroded region of the same  $\Delta m$ . The location and extent of the steel bars corrosion can be qualitatively determined by  $H_p(z)$ , apparently. All the experimental phenomena are consistent with the results of theoretical analysis, apparently.

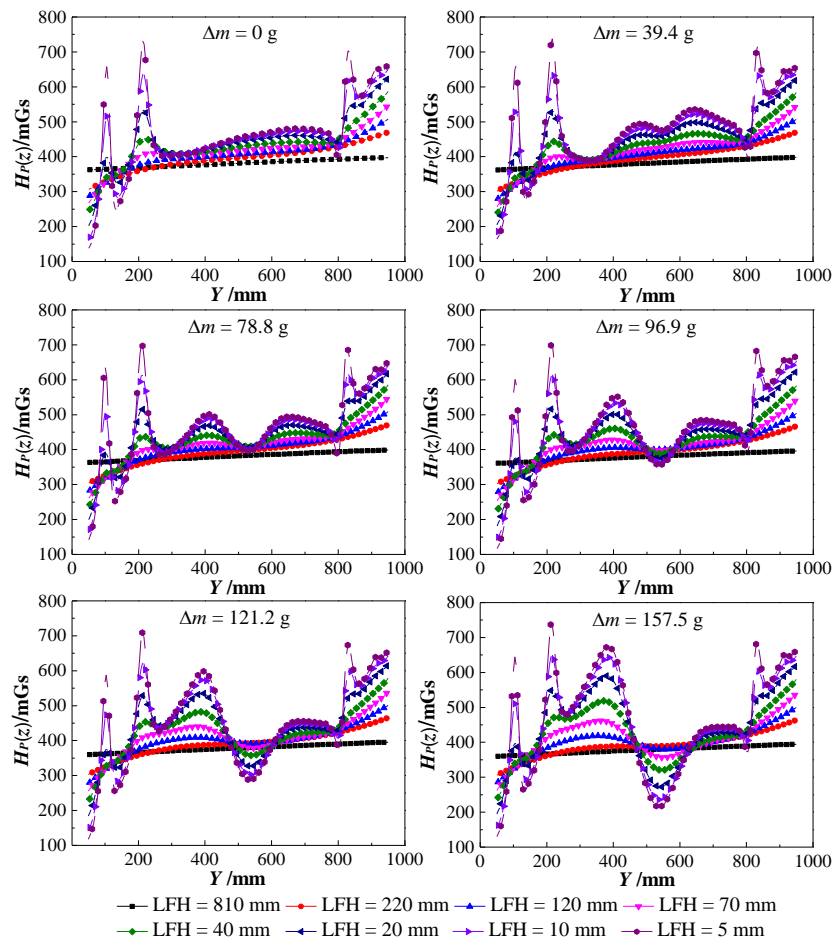


Figure 8.  $H_p(z)$  curves of the nine tested beams with different  $\Delta m$ .

In fact, the  $H_p(z)$  shown in Figure 8 is a superposition of  $H_B$ ,  $H_S$ , and  $H_E$ .  $H_B$  is the demagnetizing field of the steel bars,  $H_S$  is the SMFL field originated from the corrosion region, and  $H_E$  is the environmental magnetic field.  $H_B$  and  $H_E$  can be considered constant because the steel bars' magnetization condition and the environment had not changed during the whole experimental process, which can be confirmed by the fact the  $H_p(z)$  curves shown in Figure 8 did not significantly change within the uncorroded region. Therefore, the changes of  $H_p(z)$  within the corroded region are mainly caused by the normal component  $H_S(z)$  of the SMFL field that originated from the corrosion.

For further analysis,  $H_p(z)$  curves of each tested beam with the smallest LFH = 5 mm but different  $\Delta m$  were extracted from original  $H_p(z)$  curves shown in Figure 8. The  $H_p(z)$  curve with  $\Delta m = 0$  g is defined as the background magnetic field ( $H_B + H_E$ ), which is subtracted from each of the  $H_p(z)$  curves to obtain the  $H_S(z)$  curves originated from the corrosion region. Figure 9 shows the  $H_S(z)$  curves of 2–10 tested beams (a small number of meaningless curves that do not affect the analysis results were deleted) and the  $\Delta L$  (peak-valley spacing, unit: cm) corresponding to each  $H_S(z)$  curve. As can be seen from Figure 9, the  $H_S(z)$  curves are consistent with the theoretical analysis results, especially tested beam number four.

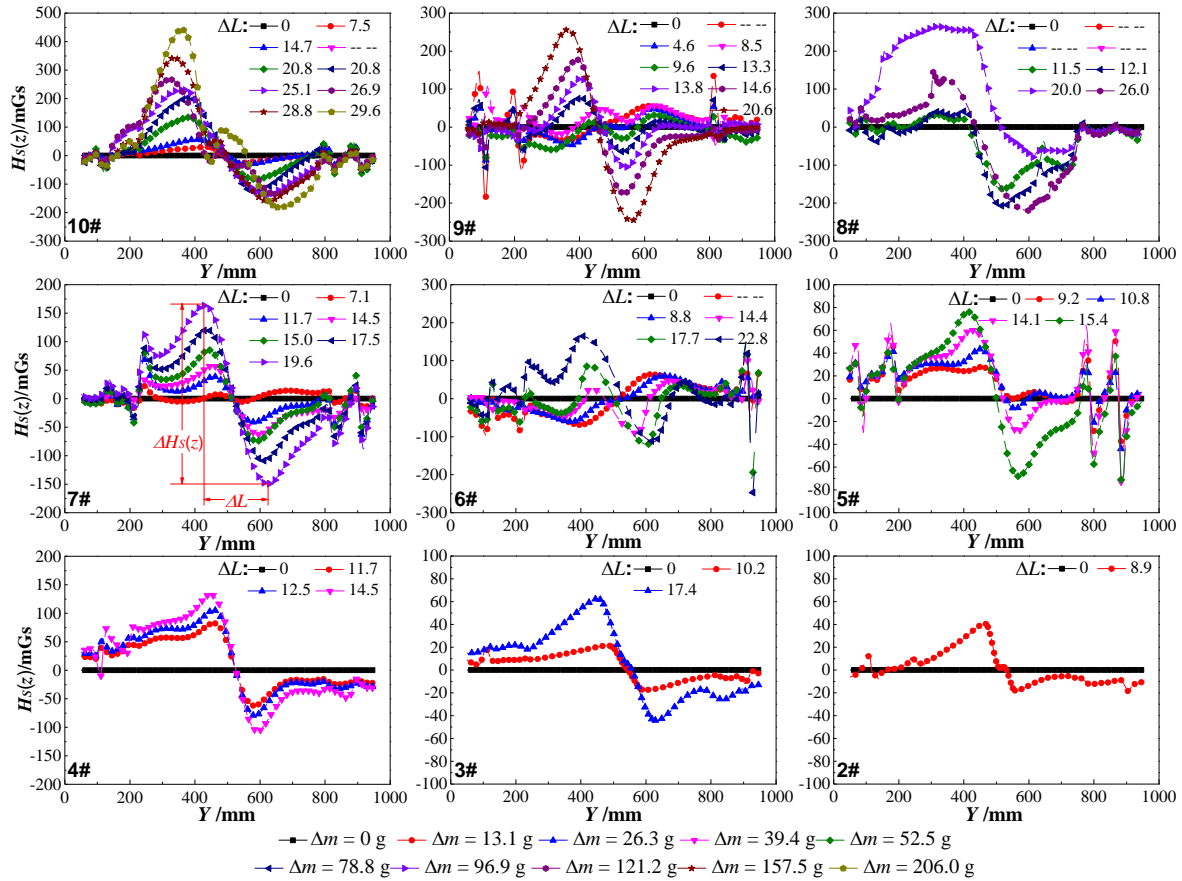


Figure 9.  $H_S(z)$  curves of 2–10 tested beam with LFH = 5 mm.

### 3.2. Analysis of SMFL Signal

In order to analyze the relationship between bending strength and SMFL signals of the corroded tested beams, the gradient  $K$  is defined.  $K$  is a direct and effective criterion for further description of the variation of SMFL signals, which is given by Equation (5):

$$K = \left| \frac{\Delta H_S(z)}{\Delta L} \right| \quad (5)$$

where  $\Delta H_S(z)$  is the difference in the values of peak and valley  $H_S(z)$  of the corroded area and  $\Delta L$  is the peak-valley spacing of  $H_S(z)$  curves, which are shown in Figure 9.

Table 3 shows the calculation parameters of gradient  $K$  of all tested beams.  $\Delta H_S(z)_{Ea}$  refers to the average value of the experimental  $\Delta H_S(z)$  with the same corrosion amount  $\Delta m$ ;  $\Delta L_{Ea}$  is that of the experimental  $\Delta L$  with the same corrosion amount  $\Delta m$ .  $R$  is the calculation cross-section remaining percentage of the corroded steel bars based on the uniform corrosion assumption, and the corrosion width  $2b$  is assumed to be 15 cm when  $R$  is calculated. The conversion model corrosion depth  $h$ , integral value  $A$ , and magnetic charge density  $\rho_{ms}$  are the theoretical calculation parameters of Equation (4). Depth  $h$  is calculated according to  $R$ , and the calculation parameters of  $A$  are  $x = 0$  cm,  $y = 7.5$  cm,  $z = 3$  cm,  $a = 2.5$  cm, and  $b = 7.5$  cm. Each  $\rho_{ms}$  is calculated according to its corresponding experimental  $\Delta H_S(z)_{Ea}$ .  $\Delta H_S(z)_T$  is the theoretical value of  $\Delta H_S(z)$ .  $K_1$  and  $K_2$  refer to the theoretical gradient and the

experimental gradient, respectively. The calculation formulas for all parameters are summarized in Equation (6):

$$\begin{cases} R = 100 \frac{15 \times \pi \times 0.7^2 \times 7.9 \times 2 - \Delta m}{15 \times \pi \times 0.7^2 \times 7.9 \times 2} = 100 - \frac{\Delta m}{3.648} \\ h = 1.4(1 - 0.01R) \\ \rho_{ms} = \frac{1}{2} \Delta H_S(z)_{Ea} \frac{4\pi\mu_0}{A} = \frac{2\pi\mu_0 \Delta H_S(z)_{Ea}}{A} \\ \Delta H_S(z)_T = 2 \frac{\rho_{ms} \cdot A}{4\pi\mu_0} = \frac{\rho_{ms} \cdot A}{2\pi\mu_0} \\ K_1 = \frac{\Delta H_S(z)_T}{2b} = \frac{\rho_{ms} \cdot A}{0.3\pi\mu_0} \\ K_2 = \frac{\Delta H_S(z)_{Ea}}{\Delta L_{Ea}} \end{cases} \quad (6)$$

Table 3. The calculation parameters of gradient K.

Parameter	$\Delta m/g$									
	0	13.1	26.3	39.4	52.5	78.8	96.9	121.2	157.5	206.2
$\Delta H_S(z)_{Ea}/mGs$	0	44.6	84.1	120.4	159.5	230.0	313.0	350.6	501.8	623.4
$\Delta L_{Ea}/cm$	-	9.1	11.5	13.2	15.0	17.2	19.6	22.5	24.7	29.6
R/%	100	96.4	92.80	89.2	85.6	78.4	73.4	66.8	56.8	43.5
h/cm	0	0.050	0.101	0.151	0.202	0.302	0.372	0.465	0.605	0.791
A	0	0.037	0.075	0.112	0.150	0.225	0.278	0.348	0.454	0.595
$\rho_{ms}/mGs$	-	7574	7046	6754	6681	6423	7074	6330	6945	6583
$\Delta H_S(z)_T/mGs$	0	40.4	81.0	121.7	162.6	244.8	302.1	377.9	493.2	646.5
$K_1/mGs \cdot m^{-1}$	0	269.5	540.0	811.6	1084	1632	2014	2520	3288	4310
$K_2/mGs \cdot m^{-1}$	0	490.1	731.3	912.1	1063	1337	1597	1558	2032	2106

Figure 10 shows the relationship diagram between K and  $\Delta m$  according to Table 3.  $K_1$  is linearly related to  $\Delta m$ , the linear fitting equation is  $K_1 = 20.8\Delta m$  with an R-squared value of 0.999.  $K_2$  is exponentially related to  $\Delta m$ , the exponential fitting equation is  $K_2 = 2204(1 - 0.985^{\Delta m})$  with an R-squared value of 0.946. The difference between  $K_1$  and  $K_2$  is mainly caused by the fact that the calculation of  $K_1$  is based on the constant assumed corrosion width, but the calculation of  $K_2$  is based on the continuous increasing actual corrosion width measured in the experiment.

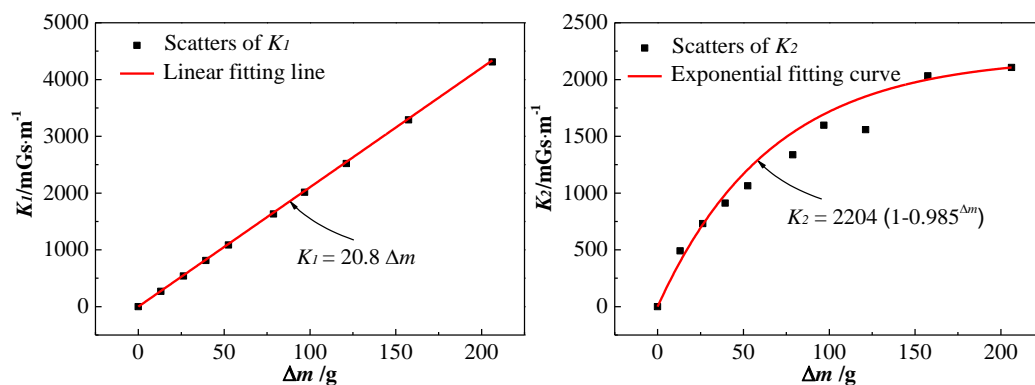


Figure 10. Diagram of relationship between K and  $\Delta m$ .

### 3.3. Analysis of Bending Strength

Table 4 shows the bending strength  $M$  and its corresponding loss rate  $S$  of all tested beams, where the theoretical bending strength  $M_1$  and the experimental bending strength  $M_2$  are calculated according to the reinforced concrete structure design principle expressed in Equation (7):

$$\begin{cases} \alpha_1 f_c b x = f_y A_s \\ M_1 = \alpha_1 f_c b x (h_0 - \frac{x}{2}) \\ A_s = 0.01AR \\ M_2 = \frac{1}{2} Fd \end{cases} \quad (7)$$

where  $\alpha_1 = 1.0$  is the simplified calculation factor,  $f_c = 14.3$  MPa is the axial compressive design strength of the concrete,  $b = 100$  mm is the section width of tested beams,  $x$  is the height of the concrete pressured zone,  $f_y = 300$  MPa is the tensile strength of the steel bar, for structure design,  $A_s$  is the total cross-sectional area of corroded steel bars,  $h_0 = 175$  mm is the effective section height,  $A = 308$  mm<sup>2</sup> is the total cross-sectional area of uncorroded steel bars,  $F$  is the loading force measured in the experiment, and  $d = 0.62$  m is the arm length of the force couple.

Figure 11 shows the relationship diagram between  $M$  and  $\Delta m$  according to Table 4. It can be seen that both  $M_1$  and  $M_2$  decrease approximately linearly with the increase of  $\Delta m$ , especially  $M_1$ . The values of  $M_2$  are not much different from that of  $M_1$ , which indicates that the results of the experiment are consistent with that of the theoretical calculation. As for the loss rate  $S$ ,  $S_1$  is positive linearly related to  $\Delta m$ , but  $S_2$  is more inclined to increase exponentially with the increase of  $\Delta m$ . The difference, mainly caused by the continuous increasing actual corrosion width in the experiment, leads to the cross-section of the steel bar being reduced more and more slowly with the same increment of  $\Delta m$ . Then,  $M_2$  decreased more and more slowly and  $S_2$  increased more and more slowly with the increase of  $\Delta m$ , which led to  $S_2$  increasing more and more slowly.

**Table 4.** The bending strength  $M$  of all tested beams.

Parameter	No.									
	1#	2#	3#	4#	5#	6#	7#	8#	9#	10#
$\Delta m/g$	0	13.1	26.3	39.4	52.5	78.8	96.9	121.2	157.5	206.0
$M_1/(KN \cdot m)$	13.2	12.8	12.3	12.0	11.6	10.8	10.2	9.5	8.2	6.5
$S_1/\%$	0	3.0	6.8	9.1	12.1	18.2	22.7	28.0	37.9	50.8
$F/kN$	48.7	42.6	40.0	39.4	38.4	35.8	32.3	27.7	24.5	23.2
$M_2/(KN \cdot m)$	15.1	13.2	12.4	12.2	11.9	11.1	10.0	8.6	7.6	7.2
$S_2/\%$	0	12.6	17.9	19.2	21.2	26.5	33.8	40.0	49.7	52.3

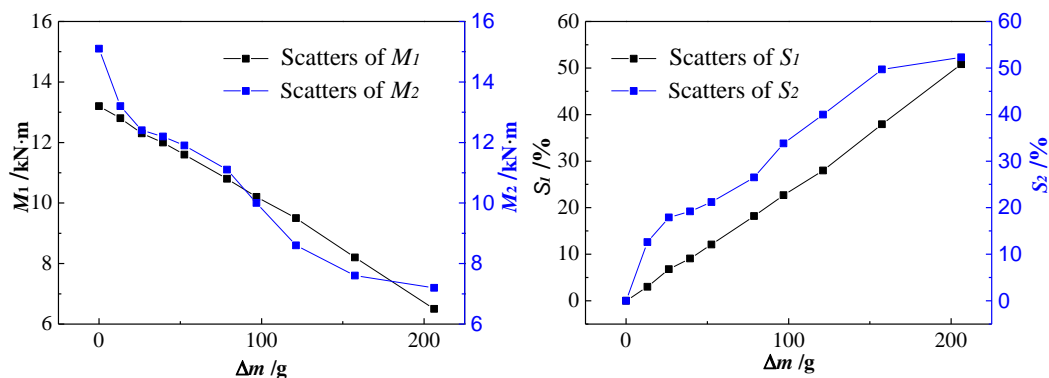


**Figure 11.** Diagram of the relationship between  $M$  and  $\Delta m$ .

### 3.4. Analysis of Relationship Between SMFL Signal and Bending Strength

According to the above analysis, both  $K$  and  $S$  increase monotonically with the increase of  $\Delta m$ . For evaluating the relationship between SMFL signals and the bending strength of the corroded reinforced concrete beams, scatters and the linear fitting line of  $S$ - $K$  are shown in Figure 12. It can be seen that with the increase of  $S_1$  and  $S_2$ , both  $K_1$  and  $K_2$  increase approximately linearly. The fitting function of the theoretical data is  $K_1 = 86.7S_1$ , with an R-squared value of 0.998, and that of the experimental data is  $K_2 = 42.4S_2$ , with an R-square value of 0.964.

Compared with the theoretical data, the experimental data is more discrete and its gradient grows more slowly. In addition to being affected by the corrosion width, this difference may originate from the fact that some factors are ignored in the idealized theoretical analysis. Such as the magnitude and the distribution of magnetic charge, meaning that the shape of the corrosion notch will be affected by nonuniform corrosion or corrosion expansion stress.

However, in general, the variation and distribution laws of  $S$ - $K$  obtained from the experiment are consistent with that of the theoretical analysis, which shows that the gradient  $K$  is a reliable and effective indicator for evaluating the residual bending strength of corroded reinforced concrete beams.

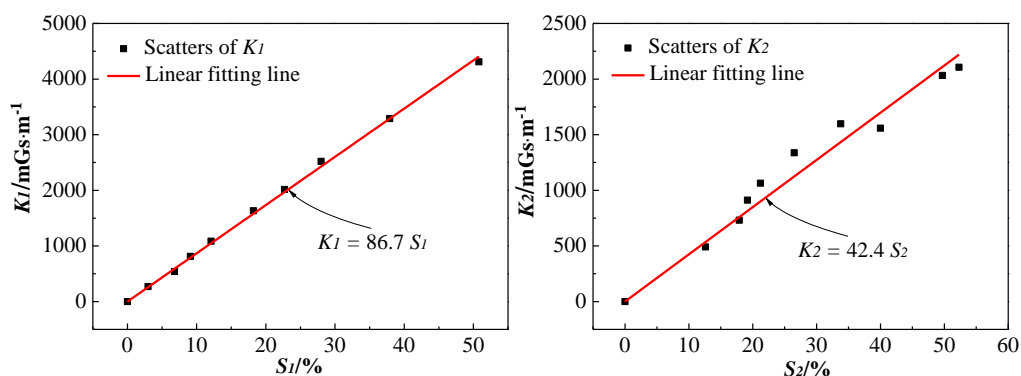


Figure 12. Scatters and linear fitting line of  $S$ - $K$ .

## 4. Conclusions

In this work, the experiment details of 10 corroded reinforced concrete tested beams based on micromagnetic sensors are introduced, followed by the derivation of the formulas of  $H_P(z)$  ( $H_S(z)$ ) based on the magnetic dipole model. Finally, both the experimental data and theoretical data were analyzed. The following conclusions can be drawn:

(1) The experimental  $H_S(z)$  curves of all tested beams are consistent with the theoretical calculation results of the magnetic dipole model, both the location and extent of the steel bars' corrosion can be qualitatively determined using  $H_S(z)$ ;

(2) The bending strength loss rate  $S$  of all the tested beams are approximately linearly related to the gradient  $K$  of  $H_S(z)$ , thus the residual bending strength of the corroded reinforced concrete beams can be evaluated based on the gradient  $K$  of  $H_S(z)$ .

This paper lays the foundation for the experimental study of the relationship between the bending strength and the SMFL signals of corroded reinforced concrete beams. A simpler, low-cost, and more efficient new method for evaluating the residual bending strength of corroded reinforced concrete beams based on the micromagnetic sensor is also proposed.

**Author Contributions:** J.Z. arranged all the work in the project and gave a keen insight in this manuscript; Y.Z. (Yingxin Zhou) and Y.Z. (Yi Zhou) investigated the current status of the research; J.Q. and R.X. derived the theoretical equations and performed the experiments; Y.Z. (Yingxin Zhou) and Y.Z. (Yi Zhou) analyzed the measured data and discussed the results; J.Q. and R.X. wrote the manuscript.

**Funding:** This research was funded by the National Key Research and Development Program of China (Grant No. 2017YFC0806007), the National Science Fund for Distinguished Young Scholars (Grant No. 51425801),

the Major Topic Special Key Research and Development Project of the Artificial Intelligence Technology Innovation in Chongqing (Grant No. cstc2017rgzn-zdyfX0018) and (cstc2017rgzn-zdyfX0029), the Science and Technology Planning Project of Yunnan Province of China (Grant Number 2017IB025), and the Science and Technology Planning Project of Nanjing of China (Grant Number 201727002).

**Conflicts of Interest:** The authors declare no conflicts of interest.

## References

- Davis, M.; Hoult, N.A.; Scott, A. Distributed strain sensing to assess corroded RC beams. *Eng. Struct.* **2017**, *6*, 473–482. [[CrossRef](#)]
- Zhao, Y.; Karimi, A.R.; Wong, H.S.; Hu, B.; Nick, R.B. Comparison of uniform and nonuniform corrosion induced damage in reinforced concrete based on a Gaussian description of the corrosion layer. *Corros. Sci.* **2011**, *53*, 2803–2814. [[CrossRef](#)]
- Yoon, I.-S. Comprehensive Approach to Calculate Oxygen Diffusivity of Cementitious Materials Considering Carbonation. *Int. J. Concr. Struct. Mater.* **2018**, *12*, 1–10. [[CrossRef](#)]
- Zhao, X.; Gong, P.; Qiao, G.; Lu, J.; Lv, X.; Ou, J. Brillouin corrosion expansion sensors for steel reinforced concrete structures using a fiber optic coil winding method. *Sensors* **2011**, *11*, 10798–10819. [[CrossRef](#)] [[PubMed](#)]
- Li, W.; Ho, S.C.M.; Song, G. Corrosion detection of steel reinforced concrete using combined carbon fiber and fiber Bragg grating active thermal probe. *Smart Mater. Struct.* **2016**, *25*, 045017. [[CrossRef](#)]
- Li, W.; Xu, C.; Ho, S.C.M.; Wang, B.; Song, G. Monitoring concrete deterioration due to reinforcement corrosion by integrating acoustic emission and FBG strain measurements. *Sensors* **2017**, *17*, 657. [[CrossRef](#)] [[PubMed](#)]
- Li, T.; Almond, D.P.; Rees, D.A.S. Crack imaging by scanning laser-line thermography and laser-spot thermography. *Meas. Sci. Technol.* **2011**, *22*, 035701. [[CrossRef](#)]
- Khodayar, F.; Lopez, F.; Ibarra-Castanedo, C.; Maldague, X. Parameter Optimization of Robotize Line Scan Thermography for CFRP Composite Inspection. *J. Nondestr. Eval.* **2018**, *37*, 5. [[CrossRef](#)]
- Khodayar, F.; Lopez, F.; Ibarra-Castanedo, C.; Maldague, X. Optimization of the inspection of large composite materials using robotized line scan thermography. *J. Nondestr. Eval.* **2017**, *36*, 32. [[CrossRef](#)]
- Gao, B.; He, Y.; Woo, W.L.; Tian, G.Y.; Liu, J.; Hu, Y. Multidimensional tensor-based inductive thermography with multiple physical fields for offshore wind turbine gear inspection. *IEEE Trans. Ind. Electron.* **2016**, *63*, 6305–6315. [[CrossRef](#)]
- Gao, B.; Lu, P.; Woo, W.L.; Tian, G.Y. Variational Bayesian Sub-group Adaptive Sparse Component Extraction for Diagnostic Imaging System. *IEEE Trans. Ind. Electron.* **2018**, *65*, 8142–8152. [[CrossRef](#)]
- Zhang, H.; Robitaille, F.; Grosse, C.U.; Ibarra-Castanedo, C.; Martins, J.O.; Sfarra, S.; Maldague, X.P.V. Optical excitation thermography for twill/plain weaves and stitched fabric dry carbon fibre preform inspection. *Composites Part: A Appl. Sci. Manuf.* **2018**, *107*, 282–293. [[CrossRef](#)]
- Sfarra, S.; Marcucci, E.; Ambrosini, D.; Paoletti, D. Infrared exploration of the architectural heritage: from passive infrared thermography to hybrid infrared thermography (HIRT) approach. *Materiales. De Construcción.* **2016**, *60*. [[CrossRef](#)]
- Grager, J.C.; Kotschate, D.; Gamper, J.; Gaal, M.; Pinkert, K.; Mooshofer, H.; Goldammer, M.; Grosse, C.U. Advances in air-coupled ultrasonic testing combining an optical microphone with novel transmitter concepts. In Proceedings of the 12th European conference on Non-Destructive Testing, Gothenburg, Sweden, 11–15 June 2018.
- Amini, M.H.; Sinclair, A.N.; Coyle, T.W. A new high-temperature ultrasonic transducer for continuous inspection. *IEEE Trans. Ultrason. Ferroelectr. Freq. Control.* **2016**, *63*, 448–455. [[CrossRef](#)] [[PubMed](#)]
- Wu, D.; Liu, Z.; Wang, X.; Su, L. Composite magnetic flux leakage detection method for pipelines using alternating magnetic field excitation. *NDT E Int.* **2017**, *91*, 148–155. [[CrossRef](#)]
- Dubov, A.A. A study of metal properties using the method of magnetic memory. *Met. Sci. Heat Treat.* **1997**, *39*, 401–405. [[CrossRef](#)]
- Piotrowski, L.; Chmielewski, M.; Augustyniak, B. On the correlation between magnetoacoustic emission and magnetostriction dependence on the applied magnetic field. *J. Magn. Magn. Mater.* **2016**, *410*, 34–40. [[CrossRef](#)]

19. Rocío, N.A.M.; Nicolás, N.; Isabel, L.P.M.; José, R.; Linilson, P. Magnetic barkhausen noise and magneto-acoustic emission in stainless steel plates. *Procedia Mater. Sci.* **2015**, *8*, 674–682. [[CrossRef](#)]
20. Wang, Z.D.; Yao, K.; Deng, B.; Ding, K.Q. Quantitative study of metal magnetic memory signal versus local stress concentration. *NDT E Int.* **2010**, *43*, 513–518. [[CrossRef](#)]
21. Coronelli, D.; Gambarova, P. Structural assessment of corroded reinforced concrete beams: modeling guidelines. *J. Struct. Eng.* **2004**, *130*, 1214–1224. [[CrossRef](#)]
22. Xia, R.; Zhou, J.; Zhang, H.; Liao, L.; Zhao, R.Q.; Zhang, Z. Quantitative Study on Corrosion of Steel Strands Based on Self-Magnetic Flux Leakage. *Sensors* **2018**, *18*, 1396. [[CrossRef](#)] [[PubMed](#)]
23. Liu, B.; He, Y.Y.; Zhang, H.; Fernandes, H.; Fu, Y.; Maldague, X. Study on characteristics of magnetic memory testing signal based on the stress concentration field. *IET Sci. Meas. Technol.* **2017**, *11*, 2–8. [[CrossRef](#)]
24. Liu, B.; Cao, Y.; Zhang, H.; Lin, Y.R.; Sun, W.R.; Xu, B. Weak magnetic flux leakage: A possible method for studying pipeline defects located either inside or outside the structures. *NDT E Int.* **2015**, *74*, 81–86. [[CrossRef](#)]
25. Liu, B.; He, L.; Zhang, H.; Cao, Y.; Fernandes, H. The axial crack testing model for long distance oil-gas pipeline based on magnetic flux leakage internal inspection method. *Measurement* **2017**, *103*, 275–282. [[CrossRef](#)]
26. Zhang, H.; Liao, L.; Zhao, R.Q.; Zhou, J.; Yang, M.; Xia, R. The nondestructive test of steel corrosion in reinforced concrete bridges using a micromagnetic sensor. *Sensors* **2016**, *16*, 1439. [[CrossRef](#)] [[PubMed](#)]
27. Zhang, H.; Liao, L.; Zhao, R.Q.; Zhou, J.; Yang, M.; Zhao, Y. A new judging criterion for corrosion testing of reinforced concrete based on self-magnetic flux leakage. *Int. J. Appl. Electromagnet Mech.* **2017**, *54*, 123–130. [[CrossRef](#)]
28. Zhang, J.; Liu, C.; Sun, M.; Li, Z. An innovative corrosion evaluation technique for reinforced concrete structures using magnetic sensors. *Constr. Build. Mater.* **2017**, *135*, 68–75. [[CrossRef](#)]
29. Polydorides, N.; Georghiou, G.E.; Kim, D.H.; Won, C. Subspace constrained regularization for corrosion detection with magnetic induction tomography. *NDT & E Int.* **2008**, *41*, 510–516.
30. Sun, B.; Dong, P.; Wang, C.; Pu, X.; Wu, Y. Quantitative analysis of magnetic anomaly of reinforcements in bored in situ concrete piles<sup>3R</sup>. *Appl. Geophys.* **2009**, *6*, 275–286. [[CrossRef](#)]
31. Orbe, A.; Rojí, E.; Losada, R.; Cuadrado, J. Calibration patterns for predicting residual strengths of steel fibre reinforced concrete (SFRC). *Composites Part. B Eng.* **2014**, *58*, 408–417. [[CrossRef](#)]
32. Krause, H.-J.; Wolf, W.; Glaas, W.; Zimmermann, E.; Faley, M.I.; Sawade, G.; Mattheus, R.; Neudert, G.; Gampe, U.; Krieger, J. SQUID array for magnetic inspection of prestressed concrete bridges. *Physica. C Supercond.* **2002**, *368*, 91–95. [[CrossRef](#)]
33. Fernandes, B.T.; Silva, I.; Gaydecki, P.A. Vector extraction from digital images of steel bars produced by an inductive scanning system using a differential gradient method combined with a modified Hough transform. *NDT E Int.* **2000**, *33*, 69–75. [[CrossRef](#)]
34. Szielasko, K.; Youssef, S.; Sourkov, A.; Kurz, J.; Pushkarev, S.; Birringer, R. Magnetic flux leakage detection of corrosion damage in prestressed concrete poles. *Electromagnetic Nondestruct. Eval. (XVIII)* **2015**, *40*, 203–210.
35. Ahmad, S. Reinforcement corrosion in concrete structures, its monitoring and service life prediction—A review. *Cem. Concr. Compos.* **2003**, *25*, 459–471. [[CrossRef](#)]
36. Huang, H.; Yao, J.; Li, Z.; Liu, Z. Residual magnetic field variation induced by applied magnetic field and cyclic tensile stress. *NDT E Int.* **2014**, *63*, 38–42. [[CrossRef](#)]

